Constraining scalar leptoquarks using COHERENT data

Roberta Calabrese [1,2,*] Jacob Gunn [1,2,†] Gennaro Miele [1,2,3,‡] Stefano Morisi [1,2,§]
Samiran Roy [2,∥] and Pietro Santorelli [1,2,¶]

[1]*Dipartimento di Fisica "Ettore Pancini", Università degli studi di Napoli "Federico II",
Complesso Univ. Monte S. Angelo, I-80126 Napoli, Italy*
[2]*INFN—Sezione di Napoli, Complesso Univ. Monte S. Angelo, I-80126 Napoli, Italy*
[3]*Scuola Superiore Meridionale, Università degli studi di Napoli "Federico II",
Largo San Marcellino 10, 80138 Napoli, Italy*

Neutrino-nucleus coherent scattering measurements by the COHERENT collaboration provide us with a unique capability to test various beyond the standard model scenarios. In this work, we constrain scalar leptoquarks (LQs) using the COHERENT data. LQs arise in many extensions of the Standard Model (SM). Generally, the mass of the LQs is assumed to be very high to avoid the bounds from proton decay. However, there are low-scale LQ models which prohibit proton decay by construction. We consider two electroweak doublet scalar LQ models with hypercharge Y = 1/6, and Y = 7/6 and provide the bounds in the plane of the Yukawa coupling and the mass of LQ. We also compare the bounds on LQs coming from various other experiments and find that the COHERENT one covers a wide range of LQ masses from MeV to TeV and in certain regions the constraints are competitive with the others.

I. INTRODUCTION

The detection of coherent elastic neutrino-nucleus scattering (CEνNS) was finally achieved by the COHERENT collaboration [1] more than forty years after it was predicted by Freedman [2]. The cross section of CEνNS events depends on the momentum transfer to the nucleus (q^2), and scales approximately as the square of the total number of protons (Z) and neutrons (N) in the target nucleus for low q^2. In the Standard Model (SM), CEνNS is mediated by the Z-boson, which couples preferentially to the neutron. Hence, the SM coherent cross section depends mainly on the square of N. The signals observed by the COHERENT collaboration show no significant deviation from the SM prediction, for CsI [1,3] and Ar [4] nuclei.

The COHERENT data presents an opportunity to verify the SM parameters at low energy scales ($\sim$10 MeV); in this energy range, the weak mixing angles can be evaluated [5–7] as well as the root mean square radii of the neutron in Cesium, Iodide, and Argon [5,6,8,9]. Furthermore, the COHERENT data is also sensitive to a plethora of new physics scenarios, such as extra mediators [10–21], nonstandard neutrino interactions (NSI) [5,22–30], generalized neutrino interactions [31,32], neutrino magnetic moments [33], nonunitarity of the leptonic mixing matrix [34], light sterile neutrinos [31,34–36], dipole portal [37,38], electromagnetic properties of neutrinos [39], fermionic dark matter [40–42], light scalar coupling to both neutrino and quarks [43], etc. For a wider review the reader is referred to [21,39]. In this work, we focus on leptoquark (LQ) models.

LQs are particles beyond the SM, carrying both lepton and baryon numbers, that in general can be scalar or vector. Here we focus on the scalar LQs case which is less constrained compared to the vector one [44–46]. Indeed vector LQs couplings are fixed from the gauge structure and there is less freedom. They arise in a large variety of beyond the SM scenarios, such as grand unified theories [47–49], the Pati-Salam model [50], extended technicolor models [51–53], etc. In general, the mass of such LQs are expected to be close to the grand unified theory (GUT) scale to avoid proton decay. There are however models with low scale LQs [54–57] which forbid rapid proton decays. We consider scalar LQs which do not give rise to tree level interactions of the type ($qlqq$), so proton decay does not occur.

---
[*]rcalabrese@na.infn.it
[†]jacobwilliam.gunn@unina.it
[‡]gennaro.miele@unina.it
[§]smorisi@na.infn.it
[∥]samroy@na.infn.it
[¶]Pietro.Santorelli@na.infn.it

The bounds on LQs via CEνNS using the effective field theory approach is discussed in [58]. In contrast, we utilize the most recent data of CsI, and the data of Ar to derive the exclusion limits on scalar LQs via modification to the SM CEνNS event rate in the presence of LQs over a wide mass range from MeV to TeV scales. We also mention interesting features of the constraints and compare our results with existing bounds on LQs. Additional constraints on LQs can be found in [59,60]. However, we mention only those constraints which are relevant to our scenarios.

The structure of this paper is as follows: Sec. II details our model and notation and provides the relevant part of the Lagrangian that mediates the coherent process. In Sec. III, we describe CEνNS SM and LQ signal predictions. Section IV contains the χ^2 analysis. In Sec. V, we report on our exclusion limits and some discussion. Finally, Sec. VI contains our conclusions.

II. MODELS

LQs couple to quarks and leptons. Therefore, LQ quantum numbers are not arbitrary and must be fixed accordingly. In Table I, we give the $SU(2)_L \times U(1)_Y$ quantum numbers of all possible terms involving quarks, leptons and a scalar LQ. The above table does not exhaustively report the possible LQ interactions which also include "diquark" type interactions for S_3, S_1, and $\tilde{S}_1$. $\tilde{R}_2$ and R_2 do not contain any "diquark" type interactions which cause proton decay [61]. Note that the term $H\tilde{R}\tilde{R}\tilde{R}$, may cause proton decay($p \rightarrow \pi^+ + \pi^- + e^- + \nu\nu$) [62], however in Refs. [63–65] it is shown that such an operator vanishes for $\tilde{R}$. For simplicity, we consider each LQ separately and do not analyze the scenarios with two LQs simultaneously. The SM Lagrangian is minimally extended to include the Yukawa interaction of the LQs with the quark and lepton fields. The relevant part of the Lagrangian that contributes in the neutrino-nucleon coherent process is given by

TABLE I. The first column corresponds to the list of $q\ell$ interaction terms. The second column shows the quantum numbers of the $q\ell$ terms. In the third column, we report the LQ quantum numbers. For more details, see Ref. [61].

	$SU(3)_c \times SU(2)_L \times U(1)_Y$	LQ
$(\overline{Q^c}_L)^i L_L^j$	$(\mathbf{3}, \mathbf{3}, -\mathbf{1/3})$	$S_3(\bar{\mathbf{3}}, \mathbf{3}, \mathbf{1/3})$
$(\overline{Q^c}_L)^i L_L^j$	$(\mathbf{3}, \mathbf{1}, -\mathbf{1/3})$	$S_1(\bar{\mathbf{3}}, \mathbf{1}, \mathbf{1/3})$
$(\overline{u^c}_R)^i \ell_R^j$	$(\mathbf{3}, \mathbf{1}, -\mathbf{1/3})$	$S_1(\bar{\mathbf{3}}, \mathbf{1}, \mathbf{1/3})$
$\bar{u}_R^i L_L^j$	$(\bar{\mathbf{3}}, \mathbf{2}, -\mathbf{7/6})$	$R_2(\mathbf{3}, \mathbf{2}, \mathbf{7/6})$
$\bar{\ell}_R^i Q_L^j$	$(\bar{\mathbf{3}}, \mathbf{2}, -\mathbf{7/6})$	$R_2(\mathbf{3}, \mathbf{2}, \mathbf{7/6})$
$\bar{d}_R^i L_L^j$	$(\bar{\mathbf{3}}, \mathbf{2}, -\mathbf{1/6})$	$\tilde{R}_2(\mathbf{3}, \mathbf{2}, \mathbf{1/6})$
$(\overline{d^c}_R)^i \ell_R^j$	$(\mathbf{3}, \mathbf{1}, -\mathbf{4/3})$	$\tilde{S}_1(\bar{\mathbf{3}}, \mathbf{1}, \mathbf{4/3})$

$$\mathcal{L}^{\Delta_1} \supset -y_{ij}^{(1)} \bar{d}_R^i \tilde{R}_2 L_L^j + \text{h.c.}$$
$$= -y_{ij}^{(1)} \bar{d}^i P_L \ell^j \Delta_1^{2/3} - y_{ij}^{(1)} \bar{d}^i P_L \nu^j \Delta_1^{-1/3} + \text{h.c.} \quad (1)$$

and

$$\mathcal{L}^{\Delta_2} \supset -y_{ij}^{(2)} \bar{u}_R^i R_2 L_L^j + \text{h.c.}$$
$$= -y_{ij}^{(2)} \bar{u}^i P_L \ell^j \Delta_2^{5/3} - y_{ij}^{(2)} \bar{u}^i P_L \nu^j \Delta_2^{2/3} + \text{h.c.}, \quad (2)$$

where $\tilde{R}_2 = (\Delta_1^{2/3}, \Delta_1^{-1/3})^T$ and $R_2 = (\Delta_2^{5/3}, \Delta_2^{2/3})^T$ under $SU(2)_L$, i, j are generation indices, d^i and u^i are the down-type and up-type quark fields, l_L^j are the lepton doublets $L_L^j = (\nu^j \ \ell^j)^T$, $P_{L,R}$, are the usual left and right chiral projection operators and y's are the Yukawa coupling matrices. The masses of LQs in the doublet structure could be different in general. However, substantial mass splitting generates large corrections to T parameter [66]. To evade such constraint, the small mass splitting ($\ll m_W$) is preferable. In that scenario, the constraint on $\Delta_1^{2/3}$ ($\Delta_2^{5/3}$) is directly bound the parameters of the Yukawa matrix y^1 (y^2) as well. Since CEνNS involves quark mass eigenstates and neutrino interaction eigenstates, the coupling matrices we are interested in are $\tilde{y}^{(1)} = V_d^\dagger y^{(1)}$ and $\tilde{y}^{(2)} = V_u^\dagger y^{(2)}$ where V_d (V_u) are arbitrary, unitary matrices which rotate the quark fields into their mass basis. Therefore, since $y^{(1)}$ [$y^{(2)}$] are arbitrary matrices, $\tilde{y}^{(1)}$ [$\tilde{y}^{(2)}$] are also completely arbitrary *a priori*. To avoid having flavor changing neutral current (FCNC) problems at tree level, we consider only couplings with the first generation of quarks. This choice does not affect our prediction for the CEνNS since it only involves the valence quarks, hence only the first generation.

In principle, one should also include terms like

$$\mathcal{L} \supset y_{ij}^{(3)} \bar{\ell}_R^i (R_2^*)^a (Q_L^j)^a + \text{h.c.} \quad (3)$$

Such terms do not contribute to CEνNS but can modify the pion decay. There are strong constraint on LQ coming from pion decay if we consider simultaneously both the Eq. (2) and Eq. (3) type operators [59]. We assume the coupling in Eq. (3) to be very small and explore the COHERENT data to constrain the couplings in Eqs. (1) and (2).

III. SIGNAL PREDICTION IN COHERENT

In this section, we present the signal prediction at COHERENT for both the SM and LQs scenarios.

At the COHERENT experiment, the neutrino fluxes come from the Spallation Neutron Source (SNS). Prompt pion decay ($\pi^+ \rightarrow \mu^+ + \nu_\mu$) at rest and the subsequently delayed decay of muons ($\mu^+ \rightarrow e^+ + \nu_e + \bar{\nu}_\mu$) produce three different neutrino fluxes. The ν_μ reach the detector within ~1.5 μs after protons-on-target while the $\bar{\nu}_\mu$ and ν_e fluxes

arrive in a comparatively longer time interval ($\sim$10 μs). The differential fluxes for neutrinos are as follows:

$$\frac{dN_{\nu_\mu}}{dE} = \eta \delta\left(E - \frac{m_\pi^2 - m_\mu^2}{2m_\pi}\right) \quad (4)$$

$$\frac{dN_{\bar{\nu}_\mu}}{dE} = \eta \frac{64E^2}{m_\mu^3}\left(\frac{3}{4} - \frac{E}{m_\mu}\right) \quad (5)$$

$$\frac{dN_{\nu_e}}{dE} = \eta \frac{192E^2}{m_\mu^3}\left(\frac{1}{2} - \frac{E}{m_\mu}\right), \quad (6)$$

where m_μ and m_π are the muon and pion masses respectively, $\eta = r N_{\text{POT}}/4\pi L^2$ is a normalization factor, N_{POT} is the total number of protons on target (POT), r corresponds to neutrinos per flavor produced for each POT, and L measures the distance between the source and the detector. For the CsI detector $r = 0.08$, $N_{\text{POT}} = 3.198 \times 10^{23}$ and L = 19.3 m [3] while for Ar $r = (9 \pm 0.9) \times 10^{-2}$, $N_{\text{POT}} = 13.7 \times 10^{22}$, L = 27.5 m.

The *SM contribution* to the CEνNS cross section for a neutrino (ν_l) as a function of the nuclear recoil kinetic energy (T_{nr}) is given by

$$\frac{d\sigma_{\nu_l-N}}{dT_{\text{nr}}}(E, T_{\text{nr}}) = \frac{G_F^2 M}{\pi}\left(1 - \frac{MT_{\text{nr}}}{2E^2}\right)Q_{l,\text{SM}}^2. \quad (7)$$

In the above, l is the neutrino flavor index, M is the mass of the detector nucleus with Z protons and N neutrons, and E is the energy of incoming neutrino, G_F is the Fermi constant, and

$$Q_{l,\text{SM}}^2 = [g_V^p(\nu_l)ZF_Z(|\vec{q}|^2) + g_V^n NF_N(|\vec{q}|^2)]^2. \quad (8)$$

Considering the radiative corrections in the minimal subtraction, $\overline{\text{MS}}$ scheme, the values of the g_V^p and g_V^n couplings are [39,67]

$$g_V^p(\nu_e) = 0.0401, \quad g_V^p(\nu_\mu) = 0.0318, \quad g_V^n = -0.5094. \quad (9)$$

The proton and neutron distributions in the nucleus are represented by the form factors [$F_Z(|\vec{q}|^2)$ and $F_N(|\vec{q}|^2)$] which depend on the three-momentum transfer $|\vec{q}| \simeq \sqrt{2MT_{\text{nr}}}$. We use the Helm parametrization [68] for the form factors[1]

$$F(|\vec{q}|^2) = 3\frac{j_1(|\vec{q}|R_0)}{|\vec{q}|R_0}e^{-|\vec{q}|^2 s^2/2}, \quad (10)$$

---

[1]The form factor of various materials relevant to CEνNS events using the large-scale nuclear shell model is discussed in [69].

where $j_1(x) = \sin(x)/x^2 - \cos(x)/x$ is the spherical Bessel function and $s = 0.9$ fm, and the rms radius R is related to R_0 by $R_{p,n}^2 = 3R_0^2/5 + 3s^2$. Helm's form factors are effectively identical to the Fermi parametrization for our purposes [26]. We take $R_p(\text{Cs}) = 4.804$ fm and $R_p(\text{I}) = 4.749$ fm as the rms radius of the proton [70,71] in CsI. For Argon, $R_p(\text{Ar}) = 3.448$ fm. The neutron rms radius is not known with good accuracy for CsI or Ar. In our analysis, we take the values $R_n(\text{Cs}) = 5.01$ fm and $R_n(\text{I}) = 4.94$ fm [72] For Argon, we use the predicted difference between the neutron and proton radii, the so-called neutron skin. Since most models predict a skin around 0.1 fm [73–75] we take $R_n(\text{Ar}) = 3.55$ fm. If the transfer of momentum is such that $|\vec{q}|R_p \gtrsim 1$ and $|\vec{q}|R_n \gtrsim 1$, the scattering loses coherence. The number of events in the ith bin of nuclear-recoil energy is given by

$$N_i^{\text{CE}\nu\text{NS}} = N(\mathcal{N})\int_{T_{\text{nr}}^i}^{T_{\text{nr}}^{i+1}} dT_{\text{nr}}A(T_{\text{nr}})\int_{E_{\min}}^{E_{\max}} dE$$
$$\times \sum_{\nu=\nu_e,\nu_\mu,\bar{\nu}_\mu}\frac{dN_\nu}{dE}\frac{d\sigma_{\nu-\mathcal{N}}}{dT_{\text{nr}}}(E, T_{\text{nr}}), \quad (11)$$

where $E_{\min} = \sqrt{MT_{\text{nr}}/2}$, $E_{\max} = m_\mu/2$–52.8 MeV, and $A(T_{\text{nr}})$ is the energy-dependent reconstruction efficiency. The nuclear recoil energy T_{nr} [keV] is converted into the corresponding electron recoil energy T_{ee} [keV]. For CsI

$$T_{ee} = (1 - \alpha_3)f_Q(T_{\text{nr}})T_{\text{nr}}, \quad (12)$$

where f_Q is the quenching factor, which we take from [76], and α_3 is a nuisance parameter quantifying the uncertainty on f_Q. For Argon

$$T_{ee} = f_Q(T_{\text{nr}})T_{\text{nr}}. \quad (13)$$

where the quenching factor is parametrized as

$$f_Q = (0.246 \pm 0.006 \text{ keV}) + ((7.8 \pm 0.9) \times 10^{-4})T_{\text{nr}}, \quad (14)$$

following [4], for 0 keV $< T_{\text{nr}} < 125$ keV. For larger energies f_Q is a constant. $N(\mathcal{N})$ is the total number of atoms present in the active detector mass (M_{det}) and $N(\mathcal{N}) = N_A M_{\text{det}}/M_{\mathcal{N}}$, where N_A is Avogadro's number and $M_{\mathcal{N}}$ is the molar mass of the detector material. For CsI we take $M_{\text{det}} = 14.6$ kg and $M_{\text{CsI}} = 259.8$ g/mol and for Ar we take $M_{\text{det}} = 24$ kg, and $M_{\text{Ar}} = 39.96$ for Ar^{40}.

In the presence of LQs the standard CEνNS cross section will be modified. Processes contributing to the CEνNS are shown Fig. 1. In this figure we can see that we have vertices with a neutrino, LQ, and a quark. As the typical momentum transfer to the nucleus is the order of a few tens of MeV,
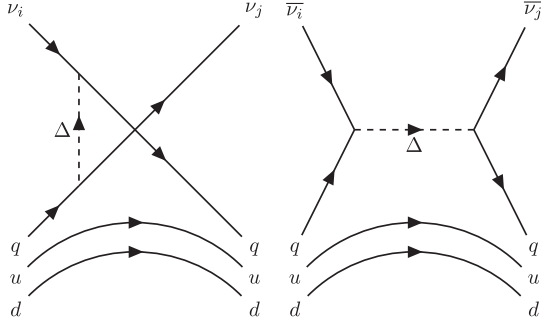
FIG. 1. Tree level processes involving the leptoquark which modifies the SM prediction for the CEνNS cross-section. The final state neutral lepton flavor is not experimentally distinguishable.

these diagrams can be represented by the effective four fermion interaction for $m_\Delta \gtrsim 10$ MeV like

$$\mathcal{L}_{\text{eff}}^\Delta = \frac{y^2}{m_\Delta^2}(\bar{\psi}_N P_L \nu)(\bar{\nu} P_R \psi_N), \tag{15}$$

where ψ_N is either a u or d quark field. However, we need to factorize this diagram into a neutrino current and a hadronic current to compute the CEνNS events. This can be achieved through Fierz transformations giving the following effective interaction

$$\mathcal{L}_{\text{eff}}^\Delta \sim -\frac{y^2}{2m_\Delta^2}(\bar{\psi}_N \gamma^\mu P_R \psi_N)(\bar{\nu}\gamma_\mu P_L \nu). \tag{16}$$

Writing the effective interaction in this way, with a $V - A$ axial structure, allows us to write down the CEνNS cross section including the contribution from LQs

$$\frac{d\sigma_{\nu_i - N}}{dT_{\text{nr}}}(E, T_{\text{nr}}) = \frac{G_F^2 M}{\pi}\left(1 - \frac{MT_{\text{nr}}}{2E^2}\right)Q_{i,k}^2 \tag{17}$$

$$Q_{i,k}^2 = \left((Q_{i,\text{SM}} + Q_{ii,\Delta_k})^2 + \sum_{j \neq i} Q_{ij,\Delta_k}^2\right) \tag{18}$$

where

$$Q_{ij,\Delta_1} = \frac{\tilde{y}_{1i}^{(1)}\tilde{y}_{1j}^{(1)}}{4\sqrt{2}G_F}\frac{ZF_Z(|\vec{q}|^2) + 2NF_N(|\vec{q}|^2)}{|\vec{q}|^2 + m_{\Delta_1^{-1/3}}^2},$$

$$Q_{ij,\Delta_2} = \frac{\tilde{y}_{1i}^{(2)}\tilde{y}_{1j}^{(2)}}{4\sqrt{2}G_F}\frac{2ZF_Z(|\vec{q}|^2) + NF_N(|\vec{q}|^2)}{|\vec{q}|^2 + m_{\Delta_2^{2/3}}^2}. \tag{19}$$

Note that typical $U'(1)$ based models [13] consider the processes like $N + \nu_i \to N + \nu_i$ for CEνNS. On the contrary here we have $N + \nu_i \to N + \nu_j$ where i can be different from j as can be seen from Fig. 1.

IV. ANALYSIS

A. CsI

Using Eqs. (7), (17), (18), (19), we compute the theoretical prediction for the event number of CEνNS assuming only the SM or assuming the existence of either Δ_1 or Δ_2. As mentioned above, we are considering the LQs that couple only to the first generation of quarks since CEνNS is sensitive only to valence quarks. Moreover, this prevents us from having FCNC at tree level mediated by LQs. For each LQ, we consider three possible scenarios. Δ_k couples to both ν_e and ν_μ (case A) or Δ_k couples only to one of ν_μ and ν_e (Case B and C) as summarized in Table II. It is possible to consider other possibilities, but they are less conservative.

To compare our predictions with the measured event rate, we need to write our prediction as a function of the photoelectron number instead of the nuclear recoil energy. In Ref. [77], it is shown that

$$N_{\text{PE}} = Y_T T_{ee}, \tag{20}$$

where $Y_T = 13.35\,N_{\text{PE}}/\text{keV}$ is the light yield of the photo-tubes. Equation (11) can be rewritten in terms of N_{PE} as

$$N_i^{\text{CE}\nu\text{NS}} = N(\mathcal{N})\int_{N_{\text{PE}}^i}^{N_{\text{PE}}^{i+1}}dN_{\text{PE}}f(N_{\text{PE}})\int_{E_{\min}}^{E_{\max}}dE$$
$$\times \sum_{\nu = \nu_e, \nu_\mu, \bar{\nu}_\mu}\frac{dN_\nu}{dE}\frac{d\sigma_{\nu-\mathcal{N}}}{dT_{\text{nr}}}(E, T_{\text{nr}}), \tag{21}$$

TABLE II. In the table we report the benchmark cases studied in this paper.

LQ	Case A			Case B			Case C		
$\Delta_1^{-1/3}$	$\tilde{y}^{(1)} = \begin{pmatrix} g_{\Delta_1} & g_{\Delta_1} & 0 \\ 0 & 0 & 0 \\ 0 & 0 & 0 \end{pmatrix}$			$\tilde{y}^{(1)} = \begin{pmatrix} 0 & g_{\Delta_1} & 0 \\ 0 & 0 & 0 \\ 0 & 0 & 0 \end{pmatrix}$			$\tilde{y}^{(1)} = \begin{pmatrix} g_{\Delta_1} & 0 & 0 \\ 0 & 0 & 0 \\ 0 & 0 & 0 \end{pmatrix}$		
$\Delta_2^{2/3}$	$\tilde{y}^{(2)} = \begin{pmatrix} g_{\Delta_2} & g_{\Delta_2} & 0 \\ 0 & 0 & 0 \\ 0 & 0 & 0 \end{pmatrix}$			$\tilde{y}^{(2)} = \begin{pmatrix} 0 & g_{\Delta_2} & 0 \\ 0 & 0 & 0 \\ 0 & 0 & 0 \end{pmatrix}$			$\tilde{y}^{(2)} = \begin{pmatrix} g_{\Delta_2} & 0 & 0 \\ 0 & 0 & 0 \\ 0 & 0 & 0 \end{pmatrix}$		

where $f(N_{\mathrm{PE}})$ is the detector efficiency in terms of the photoelectron content defined as [3]

$$f(x) = \frac{a}{1 + \exp(-k(x - x_0))} + d, \qquad (22)$$

where

$$\begin{aligned}
a &= 1.32045 \pm 0.02345, \\
k &= 0.2859792 \pm 0.000613, \\
x_0 &= 10.8646 \pm 1.0186, \\
d &= -0.333322 \pm 0.023042. \qquad (23)
\end{aligned}$$

In Fig. 2, we compare the COHERENT CEνNS event rate, in cyan, to the SM prediction in black, and our case A model predictions in violet and orange. The plot shows the event per photoelectron. To get the number of events measured, one has to multiply the height and width of each bin. Since $Q_{i,\mathrm{SM}}$ and Q_{ii,Δ_k} have opposite sign, the resulting event rate can be higher or smaller than the SM one depending on $(g_{\Delta_{1,2}}, m_{\Delta_{1,2}})$.

To constrain the models, we perform a χ^2 analysis analogous to that in Ref. [13]

$$\chi^2 = \min_{\boldsymbol{\alpha}} \sum_{i=4}^{15} \left[\left(\frac{N_i^{\mathrm{exp}} - (1 + \alpha_1)N_i^{\mathrm{CE}\nu\mathrm{NS}} - (1 + \alpha_2)B_i}{\sigma_i} \right)^2 + \sum_j \left(\frac{\alpha_j}{\sigma_{\alpha_j}} \right)^2 \right]. \qquad (24)$$

For each bin i, we indicate with N_i^{exp} the measured event number reported in Ref. [3], $N_i^{\mathrm{CE}\nu\mathrm{NS}}$ is the expected event
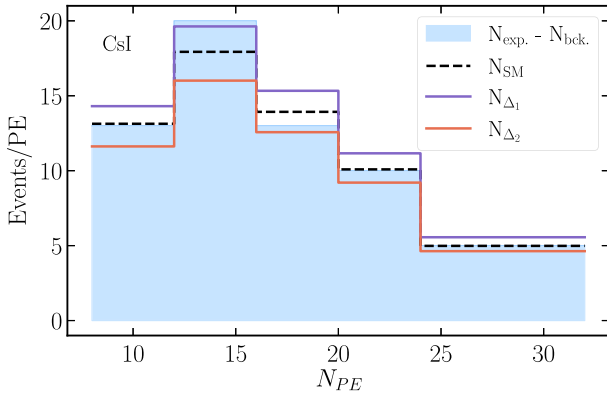

FIG. 2. The plot shows the number of events vs the photoelectron number. The difference between experimental and the background event rate is presented in cyan. The dashed black line represents the SM event prediction, the violet solid line corresponds to the prediction including $\Delta_1^{-1/3}$, the orange solid line is the prediction for $\Delta_2^{2/3}$. The theoretical predictions for the case A (see Table II) are obtained assuming $m_\Delta = 1$ GeV and $g_\Delta = 3.5 \times 10^{-3}$.

rate, B_i is the background event rate [3], and σ_i is the statistical uncertainty taken to be equal to the square root of the event number. As done in Refs. [6,13], we consider only the energy bins from 8 to 32 photoelectrons because they span the recoil kinetic energy range covered by the most recent quenching factor measurement performed at Chicago-3 [76]. We are considering 3 nuisance parameters $\boldsymbol{\alpha} = (\alpha_1, \alpha_2, \alpha_3)$ which quantify the systematic uncertainty of the signal rate, background rate, and quenching factor respectively. The corresponding standard deviations are $\sigma_{\boldsymbol{\alpha}} = (0.112, 0.25, 0.051)$ [1].

The choices we made for the Yukawa couplings prevent us from having constraints from FCNC and B-physics. Moreover, we can overcome the constraints from LFV considering a mass splitting between the members of the doublets.

B. Argon

Analogously to the preceding analysis for CsI, using Eq. (11) we can obtain the theoretical prediction for the CEνNS event rate in the Argon detector assuming only the SM or assuming the existence of either Δ_1 or Δ_2. The energy-dependent reconstruction coefficient for Argon is also taken from analysis A in Ref. [4].

We perform the following χ^2 analysis

$$\chi^2_{\mathrm{Ar}} = \sum_{i=1}^{12} \left(\frac{N_i^{\mathrm{exp}} - (1 + \beta_1)N_i^{\mathrm{CE}\nu\mathrm{NS}} - B_i}{\sigma_i} \right)^2 + \sum_j \left(\frac{\beta_j}{\sigma_{\beta_j}} \right)^2 \qquad (25)$$

where $B_i = (1 + \beta_2)B_i^{\mathrm{PBRN}} + (1 + \beta_3)B_i^{\mathrm{LBRN}}$. PBRN means prompt beam-related background and LBRN is the late-beam-related neutron background, so that B_i^{PBRN}, B_i^{LBRN} are the estimated number of PBRN and LBRN events in the ith energy bin. In the above [4]

$$\sigma_i^2 = (\sigma_i^{\mathrm{exp}})^2 + (\sigma_{\mathrm{BRNES}}(B_i^{\mathrm{PBRN}} + B_i^{\mathrm{LBRN}}))^2 \qquad (26)$$

where $\sigma_{\mathrm{BRNES}} = 1.7\%$ and $\sigma_{\boldsymbol{\beta}} = (0.132, 0.32, 1)$ [4]. In this way, the uncertainty on the beam related neutron energy shape (BRNES) is distributed over the energy bins in an uncorrelated manner, and β_1, β_2, β_3 are the nuisance parameters which quantify the uncertainty on the signal rate and PBRN and LBRN background event rates.

V. RESULTS

We show the constraints on the Yukawa coupling strength as a function of the LQ masses in Fig. 3 for the cases described in Table II. The top and bottom panels correspond to CsI and Ar respectively, whereas the left and right panels depict the constraint on case A only, and cases B and C respectively. The constraints on $\Delta_{1,2}$ differ only at the percent level, therefore we report them as a single solid
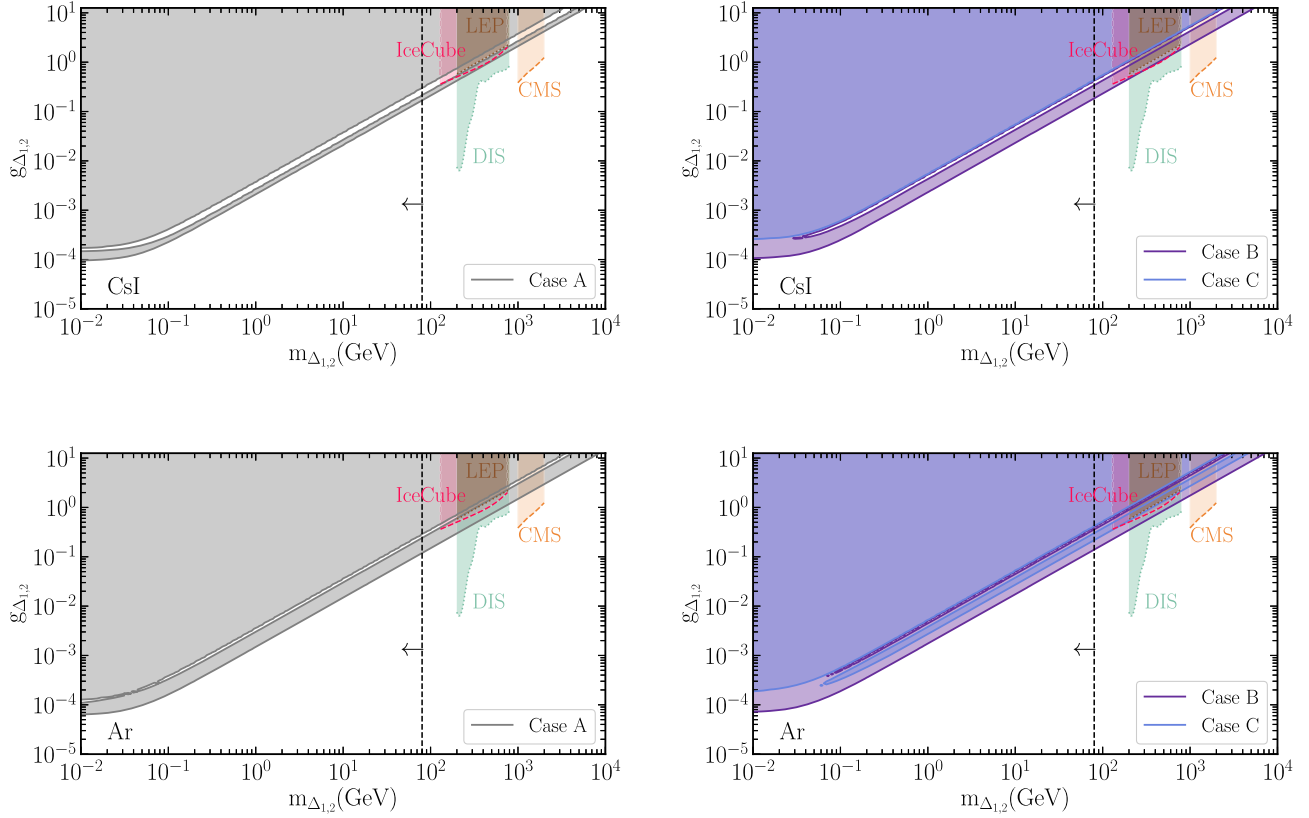
FIG. 3. Constraints obtained in the plane $g_\Delta - m_\Delta$. In the left panel, the constraints on Case A are shown, while on the right we present the constraints on Case B and C. In the upper half we show the constraints obtained using CsI, and in the lower half those from Argon. In solid colored lines we have reported the constraints at 90% C.L. obtained using our analysis. The dashed colored lines show the constraints for $\Delta_1^{-1/3}$ and $\Delta_2^{2/3}$ from CMS (in orange) [78] and IceCube (in pink) [44]. The dotted brown and green lines represent the constraints for $\Delta_1^{2/3}$ and $\Delta_2^{5/3}$. Such constraints are taken from Ref. [82].

line. Expectedly, the most stringent constraints apply to scenario A since all of the ν_μ, $\bar{\nu}_\mu$ and ν_e fluxes contribute to the CEνNS events rate, while only the $\nu_{\mu,\bar{\mu}}$ and only the ν_e participate in case B and C respectively. For very low LQs masses (around 10 MeV), the bounds become insensitive to m_Δ as in this region, the cross section depends mainly on the momentum transfer (q^2). In each plot, we show some existing constraints on LQs for comparison. The dashed lines are used for the bounds which constrain $\Delta_1^{-1/3}$ or $\Delta_2^{2/3}$, while the dotted lines correspond to those which are obtained for the other member of the doublets. The orange dashed line corresponds to constraints from CMS taken from Ref. [78], for which the LQs (Δ) are pair produced via gluon fusion and the constraints are obtained assuming BR($\Delta \to q + \nu$) = 1. A similar bound is reported using the pair production of asymmetric LQs in Ref. [79]. IceCube also provide constraints on LQs which we show in pink [44], and are discussed in Refs. [80,81]. The brown and green dotted lines show the LEP and deep inelastic scattering bounds taken from Ref. [82], which constrain the charged lepton element of the LQ doublet. A large mass

splitting of the doublet components leads to sizable correction to T parameter [66]. Hence, in the limit of degenerate LQ doublet masses, those bounds would apply to our scenarios. The low mass ($\lesssim$80 GeV) LQs are severely constrained by the LEP searches via the unsuppressed channel $e^+e^- \to \gamma^* \to \Delta^+\Delta^-$. Note that in Ref. [83], the constraint is obtained for charged Higgs but this is also applicable to charged LQs. The bound is indicated by the black dashed line. Constraints may also arise from other experimental observations, like $K^0 - \bar{K}^0$ or $D^0 - \bar{D}^0$ oscillation or in general B physics, but such constraints do not apply due to the Yukawa structure considered.

The constrained regions are not continuous due to a degeneracy of the SM and LQ contributions. In Fig. 4 we show the behavior of $\Delta\chi^2$ for $\Delta_1^{-1/3}$ obtained using Eq. (24) to illustrate the shape of the constraints. The magenta, red, and blue lines corresponds to cases A, B, and C respectively for $m_{\Delta_1} = 1$ GeV. By looking at Eqs. (8), (9) and taking the values of the form factors to one, we obtain the value of $Q_{i\mathrm{SM}} \simeq -N/2$. On the other hand, $Q_{ij,\Delta_K} > 0$.
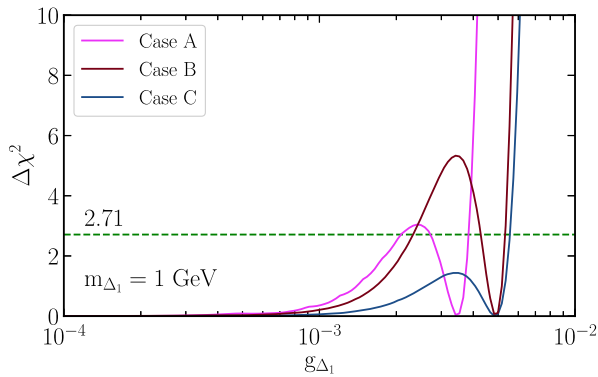
FIG. 4. $\Delta\chi^2$ vs g_{Δ_1} for $m_{\Delta_1} = 1$ GeV for CsI. In magenta, red and blue we report Case A, B, and C respectively (see Table II). The green line refers to $\Delta\chi^2 = 2.71$.

Therefore, there is a degenerate point where the total new charge approaches $N/2$. From Eq. (18), we get

$$\text{for case A:} \left(-\frac{N}{2} + Q_{ii,\Delta_K}\right)^2 + \sum_{i \neq j} Q_{ij,\Delta_K}^2 \simeq \left(\frac{N}{2}\right)^2,$$

$$\text{for case B and C:} \left(-\frac{N}{2} + Q_{ii,\Delta_K}\right)^2 \simeq \left(\frac{N}{2}\right)^2, \qquad (27)$$

which almost reproduces the SM prediction. As the ratio g_Δ/m_Δ increases from zero, the predicted event rate including LQs is initially decreasing from the SM prediction. At a certain point the prediction equals the SM one [see Eq. (27)], and the $\Delta\chi^2 = 0$. This is the degeneracy which causes the discontinuity in our constraints.

VI. CONCLUSIONS

In this work, we utilize the neutrino-nucleus coherent elastic scattering data to put bounds on scalar LQs over a wide mass range from MeV to TeV scales. We consider scalar LQs with hypercharge $Y = 1/6$ and $Y = 7/6$. These LQs do not have any "diquark" couplings which contribute to the proton decay. Hence effectively the LQ masses could be well below the GUT scale. We use a Fierz transformation to recast the effective four-fermion interaction vertex into neutrino-neutrino and quark-quark currents. This allows us to calculate the hadronic matrix elements for the coherent process. Only the valence quarks (u and d) of the nuclei participate in neutrino-nucleus coherent scattering. Therefore, we can constrain the specific structure of the Yukawa matrix that couples to the first generation of quarks, and neutrinos. Our choices of couplings evade bounds from FCNCs and LFV. Hence, COHERENT measurements allow us to probe this particular Yukawa structure. We also show the constraints coming from LHC, IceCube, LEP, and DIS. These constraints are comparable with our bounds for some mass regions. Placing constraints on LQs over a wide mass range is the unique capability of coherent neutrino-nucleus scattering measurements.

[1] D. Akimov *et al.* (COHERENT Collaboration), Science **357,** 1123 (2017).

[2] D. Z. Freedman, Phys. Rev. D **9,** 1389 (1974).

[3] D. Akimov *et al.* (COHERENT Collaboration), Phys. Rev. Lett. **129,** 081801 (2022).

[4] D. Akimov *et al.* (COHERENT Collaboration), Phys. Rev. Lett. **126,** 012002 (2021).

[5] O. G. Miranda, D. K. Papoulias, G. Sanchez Garcia, O. Sanders, M. Tórtola, and J. W. F. Valle, J. High Energy Phys. 05 (2020) 130; 01 (2021) 067(E).

[6] M. Cadeddu, F. Dordei, C. Giunti, Y. F. Li, and Y. Y. Zhang, Phys. Rev. D **101,** 033004 (2020).

[7] M. Cadeddu, N. Cargioli, F. Dordei, C. Giunti, Y. F. Li, E. Picciau, C. A. Ternes, and Y. Y. Zhang, Phys. Rev. C **104,** 065502 (2021).

[8] M. Cadeddu, C. Giunti, Y. F. Li, and Y. Y. Zhang, Phys. Rev. Lett. **120,** 072501 (2018).

[9] B. C. Canas, E. A. Garces, O. G. Miranda, A. Parada, and G. Sanchez Garcia, Phys. Rev. D **101,** 035012 (2020).

[10] B. Dutta, R. Mahapatra, L. E. Strigari, and J. W. Walker, Phys. Rev. D **93,** 013015 (2016).

[11] M. Abdullah, J. B. Dent, B. Dutta, G. L. Kane, S. Liao, and L. E. Strigari, Phys. Rev. D **98,** 015005 (2018).

[12] B. Dutta, S. Liao, S. Sinha, and L. E. Strigari, Phys. Rev. Lett. **123,** 061801 (2019).

[13] M. Cadeddu, N. Cargioli, F. Dordei, C. Giunti, Y. F. Li, E. Picciau, and Y. Y. Zhang, J. High Energy Phys. 01 (2021) 116.

[14] L. J. Flores, N. Nath, and E. Peinado, J. High Energy Phys. 06 (2020) 045.

[15] H. Banerjee, B. Dutta, and S. Roy, Phys. Rev. D **104,** 015015 (2021).

[16] L. M. G. de la Vega, L. J. Flores, N. Nath, and E. Peinado, J. High Energy Phys. 09 (2021) 146.

[17] M. Atzori Corona, M. Cadeddu, N. Cargioli, F. Dordei, C. Giunti, Y. F. Li, E. Picciau, C. A. Ternes, and Y. Y. Zhang, J. High Energy Phys. 05 (2022) 109.

[18] D. T. Binh, L. T. Hue, V. H. Binh, D. V. Soa, and H. N. Long, arXiv:2109.08118.

[19] E. Bertuzzo, G. Grilli di Cortona, and L. M. D. Ramos, J. High Energy Phys. 06 (2022) 075.

[20] K. Chakraborty, A. Das, S. Goswami, and S. Roy, J. High Energy Phys. 04 (2022) 008.

[21] V. De Romeri, O. G. Miranda, D. K. Papoulias, G. Sanchez Garcia, M. Tórtola, and J. W. F. Valle, arXiv:2211.11905.

[22] J. Barranco, O. G. Miranda, and T. I. Rashba, J. High Energy Phys. 12 (2005) 021.

[23] K. Scholberg, Phys. Rev. D **73,** 033005 (2006).

[24] M. Lindner, W. Rodejohann, and X.-J. Xu, J. High Energy Phys. 03 (2017) 097.

[25] J. Liao and D. Marfatia, Phys. Lett. B **775,** 54 (2017).

[26] C. Giunti, Phys. Rev. D **101,** 035039 (2020).

[27] P. B. Denton and J. Gehrlein, J. High Energy Phys. 04 (2021) 266.

[28] A. N. Khan, D. W. McKay, and W. Rodejohann, Phys. Rev. D **104,** 015019 (2021).

[29] P. Coloma, I. Esteban, M. C. Gonzalez-Garcia, L. Larizgoitia, F. Monrabal, and S. Palomares-Ruiz, J. High Energy Phys. 05 (2022) 037.

[30] S. S. Chatterjee, S. Lavignac, O. G. Miranda, and G. Sanchez Garcia, arXiv:2208.11771.

[31] B. Dutta, Y. Gao, R. Mahapatra, N. Mirabolfathi, L. E. Strigari, and J. W. Walker, Phys. Rev. D **94,** 093002 (2016).

[32] L. J. Flores, N. Nath, and E. Peinado, Phys. Rev. D **105,** 055010 (2022).

[33] O. G. Miranda, D. K. Papoulias, M. Tórtola, and J. W. F. Valle, J. High Energy Phys. 07 (2019) 103.

[34] O. G. Miranda, D. K. Papoulias, O. Sanders, M. Tórtola, and J. W. F. Valle, Phys. Rev. D **102,** 113014 (2020).

[35] T. S. Kosmas, D. K. Papoulias, M. Tortola, and J. W. F. Valle, Phys. Rev. D **96,** 063013 (2017).

[36] O. G. Miranda, G. Sanchez Garcia, and O. Sanders, Adv. High Energy Phys. **2019,** 3902819 (2019).

[37] A. Dasgupta, S. K. Kang, and J. E. Kim, J. High Energy Phys. 11 (2021) 120.

[38] P. D. Bolton, F. F. Deppisch, K. Fridell, J. Harz, C. Hati, and S. Kulkarni, Phys. Rev. D **106,** 035036 (2022).

[39] M. Cadeddu, F. Dordei, C. Giunti, Y. F. Li, E. Picciau, and Y. Y. Zhang, Phys. Rev. D **102,** 015030 (2020).

[40] V. Brdar, W. Rodejohann, and X.-J. Xu, J. High Energy Phys. 12 (2018) 024.

[41] J. A. Dror, G. Elor, and R. Mcgehee, Phys. Rev. Lett. **124,** 18 (2020).

[42] J. A. Dror, G. Elor, and R. Mcgehee, J. High Energy Phys. 02 (2020) 134.

[43] Y. Farzan, M. Lindner, W. Rodejohann, and X.-J. Xu, J. High Energy Phys. 05 (2018) 066.

[44] U. K. Dey and S. Mohanty, J. High Energy Phys. 04 (2016) 187.

[45] G. Valencia and S. Willenbrock, Phys. Rev. D **50,** 6843 (1994).

[46] A. D. Smirnov, Mod. Phys. Lett. A **22,** 2353 (2007).

[47] H. Georgi and S. L. Glashow, Phys. Rev. Lett. **32,** 438 (1974).

[48] H. Fritzsch and P. Minkowski, Ann. Phys. (N.Y.) **93,** 193 (1975).

[49] A. Preda, G. Senjanovic, and M. Zantedeschi, Phys. Lett. B **838,** 137746 (2023).

[50] J. C. Pati and A. Salam, Phys. Rev. D **10,** 275 (1974).

[51] E. Farhi and L. Susskind, Phys. Rep. **74,** 277 (1981).

[52] T. Gabriel, D. Groom, P. Job, N. Mokhov, and G. Stevenson, Nucl. Instrum. Methods Phys. Res., Sect. A **338,** 336 (1994).

[53] J. R. Andersen *et al.*, Eur. Phys. J. Plus **126,** 81 (2011).

[54] W. Buchmüller, R. Rückl, and D. Wyler, Phys. Lett. B **191,** 442 (1987).

[55] A. Belyaev, C. Leroy, R. Mehdiyev, and A. Pukhov, J. High Energy Phys. 09 (2005) 005.

[56] I. Dorsner and P. Fileviez Perez, Nucl. Phys. **B723,** 53 (2005).

[57] P. Fileviez Perez and M. B. Wise, Phys. Rev. D **88,** 057703 (2013).

[58] A. Crivellin, M. Hoferichter, M. Kirk, C. A. Manzari, and L. Schnell, J. High Energy Phys. 10 (2021) 221.

[59] S. Davidson, D. C. Bailey, and B. A. Campbell, Z. Phys. C **61,** 613 (1994).

[60] A. Crivellin, D. Müller, and L. Schnell, Phys. Rev. D **103,** 115023 (2021).

[61] I. Doršner, S. Fajfer, A. Greljo, J. F. Kamenik, and N. Košnik, Phys. Rep. **641,** 1 (2016).

[62] J. M. Arnold, B. Fornal, and M. B. Wise, Phys. Rev. D **87,** 075004 (2013).

[63] A. Crivellin and L. Schnell, Comput. Phys. Commun. **271,** 108188 (2022).

[64] C. Murgui and M. B. Wise, Phys. Rev. D **104,** 035017 (2021).

[65] I. Doršner, S. Fajfer, and O. Sumensari, J. High Energy Phys. 05 (2022) 183.

[66] S. Davidson and S. Descotes-Genon, J. High Energy Phys. 11 (2010) 073.

[67] J. Erler and S. Su, Prog. Part. Nucl. Phys. **71,** 119 (2013).

[68] R. H. Helm, Phys. Rev. **104,** 1466 (1956).

[69] M. Hoferichter, J. Menéndez, and A. Schwenk, Phys. Rev. D **102,** 074018 (2020).

[70] G. Fricke, C. Bernhardt, K. Heilig, L. A. Schaller, L. Schellenberg, E. B. Shera, and C. W. de Jager, At. Data Nucl. Data Tables **60,** 177 (1995).

[71] I. Angeli and K. P. Marinova, At. Data Nucl. Data Tables **99,** 69 (2013).

[72] M. Bender, K. Rutz, P. G. Reinhard, J. A. Maruhn, and W. Greiner, Phys. Rev. C **60,** 034304 (1999).

[73] P. G. Reinhard and H. Flocard, Nucl. Phys. **A584,** 467 (1995).

[74] T. Niksic, D. Vretenar, and P. Ring, Phys. Rev. C **78,** 034318 (2008).

[75] C. G. Payne, S. Bacca, G. Hagen, W. Jiang, and T. Papenbrock, Phys. Rev. C **100,** 061304 (2019).

[76] J. I. Collar, A. R. L. Kavner, and C. M. Lewis, Phys. Rev. D **100,** 033003 (2019).

[77] D. Akimov *et al.* (COHERENT Collaboration), arXiv:1804.09459.

[78] A. Tumasyan *et al.* (CMS Collaboration), J. High Energy Phys. 11 (2021) 153.

[79] I. Doršner, A. Lejlić, and S. Saad, arXiv:2210.11004.

[80] U. K. Dey, D. Kar, M. Mitra, M. Spannowsky, and A. C. Vincent, Phys. Rev. D **98**, 035014 (2018).

[81] D. Bečirević, B. Panes, O. Sumensari, and R. Zukanovich Funchal, J. High Energy Phys. 06 (2018) 032.

[82] P. Taxil, E. Tugcu, and J. M. Virey, Eur. Phys. J. C **14**, 165 (2000).

[83] G. Abbiendi *et al.* (ALEPH, DELPHI, L3, OPAL, LEP Collaborations), Eur. Phys. J. C **73**, 2463 (2013).